

Enhanced battery performance in manganese hexacyanoferrate by partial substitution

Yutaka Moritomo^{a,b,c,*}, Shota Urase^a, and Takayuki Shibata^{a,b}

^a Graduate School of Pure and Applied Science, University of Tsukuba, Tsukuba 305-8577, Japan

^b Faculty of Pure and Applied Science, University of Tsukuba, Tsukuba 305-8577, Japan

^c Center for Integrated Research in Fundamental Science and Engineering (CiRfSE), University of Tsukuba, Tsukuba 305-8577, Japan

*corresponding author (moritomo.yutaka.gf@u.tsukuba.ac.jp)

Manganese hexacyanoferrate (Mn-HCF) is a promising cathode material for sodium-ion secondary batteries (SIBs). We investigated the effects of partial substitution of Fe, Co, and Ni for Mn in Mn-HCF on the SIB rate and cycle performance. The discharge capacity is discernible at 50 C in the substituted samples, while it disappears at 20 C in the non-substituted samples. We ascribed the enhancement of the rate performance to the suppression of the Jahn-Teller distortion of Mn³⁺ and the resultant activation of the Mn reduction reaction.

Keywords:

Sodium-ion secondary battery

Cathode material

Manganese-hexacyanoferrate

Jahn-Teller instability

1. Introduction

Coordination polymers are promising cathode materials for sodium-ion secondary batteries (SIBs) because of the robust nature of their frameworks against Na^+ intercalation/deintercalation. Among the different coordination polymers, transition metal hexacyanoferrates (metal-HCF), [1] *i.e.*, $A_xM[\text{Fe}(\text{CN})_6]_y$ (A and M are alkali and transition metals, respectively), have been intensively investigated as cathode materials for SIBs. [2-11] Metal-HCFs contain a three-dimensional (3D) jungle-gym-type framework with periodic cubic nanopores 0.5 nm in size at the edge. While Goodenough's group [2] reported Na^+ intercalation behaviors in $\text{K}-M\text{-Fe}(\text{CN})_6$ systems ($M = \text{Mn}, \text{Fe}, \text{Co}, \text{Ni}, \text{Cu}, \text{Zn}$), it was found that their Coulombic efficiency is very low. The efficiency is significantly improved in thin films of $\text{Na}_{1.32}\text{Mn}^{\text{II}}[\text{Fe}^{\text{II}}(\text{CN})_6]_{0.83} \cdot 3.5\text{H}_2\text{O}$ [3] and $\text{Na}_{1.6}\text{Co}^{\text{II}}[\text{Fe}^{\text{II}}(\text{CN})_6]_{0.9} \cdot 2.9\text{H}_2\text{O}$. [4] By a structural optimization, Yang *et al.* [5] demonstrated that $\text{Na}_{1.76}\text{Ni}_{0.12}\text{Mn}_{0.88}[\text{Fe}(\text{CN})_6]_{0.98}$ exhibits an excellent cycle life. In addition, Lee *et al.* [6] reported that $\text{Na}_2\text{Mn}^{\text{II}}[\text{Mn}^{\text{II}}(\text{CN})_6]$ shows an excellent capacity of 209 mAh/g, which is mediated by one- and two-electron reactions. Wang *et al.* [7] reported that rhombohedral Prussian white, $\text{Na}_{1.92}\text{Fe}[\text{Fe}(\text{CN})_6]$, works as a cathode material.

Mn-HCF is especially interesting because it consists of ubiquitous elements only and is therefore a promising low-cost cathode material for SIBs. Takachi *et al.* [11] investigated the structural, electronic, and electrochemical properties of $\text{Na}_{1.32}\text{Mn}^{\text{II}}[\text{Fe}^{\text{II}}(\text{CN})_6]_{0.83} \cdot 3.5\text{H}_2\text{O}$ thin film electrodes. They observed discharge capacity of 135 mAh/g and ascribed it to the Mn reduction reaction ($\text{Mn}^{3+}/\text{Mn}^{2+}$) at 3.7 V and the Fe reduction reaction ($\text{Fe}^{3+}/\text{Fe}^{2+}$) at 3.3 V. The drawback of Mn-HCF is that the Jahn-Teller (JT) instability of Mn^{3+} prevents the Mn reduction reaction at a high rate. [12]

In this paper, we investigated the effects of partial substitution of Fe, Co, and Ni for Mn in Mn-HCF on the SIB rate and cycle performance. The Mn-HCF has around 10 % deficiency of $[\text{Fe}(\text{CN})_6]$ and its capacity is governed by the Na concentration (= 1.6 per a Mn site). This means that around 30% Mn site does not contribute the redox reaction: $\text{Na}_{1.6}\text{Mn}^{\text{II}}[\text{Fe}^{\text{II}}(\text{CN})_6]_{0.9} \rightarrow \text{Mn}^{\text{II}}_{0.3}\text{Mn}^{\text{III}}_{0.7}[\text{Fe}^{\text{III}}(\text{CN})_6]_{0.9} + 1.6\text{Na}^+$. Then, we can replace 20 - 30 % Mn by the other transition metals, *i.e.*, Fe, Co, and Ni, without lowering the capacity. We found that the discharge capacity is discernible even at 50 C in the substituted samples, while it disappears at 20 C in the non-substituted samples. The enhancement of the rate performance is ascribed to the activation of the Mn reduction reaction probably by the suppression of the cooperative JT distortion of Mn^{3+} .

2. Experimental

2.1 Sample preparation and characterization

We prepared Mn-HCF and Fe-, Co-, and Ni-substituted Mn-HCFs using the method of precipitation from aqueous solutions in air at 40 °C. For convenience, we denote the Fe-, Co-, and Ni-

substituted Mn-HCFs as Mn/Fe-, Mn/Co-, and Mn/Ni-HCFs, respectively. Using a tube pump, an aqueous solution (32 mM $\text{Mn}^{\text{II}}\text{Cl}_2$, 8 mM $\text{M}^{\text{II}}\text{Cl}_2$, and 4 M NaCl: $M = \text{Mn, Fe, Co, and Ni}$) was slowly mixed into a $\text{Na}_4[\text{Fe}^{\text{II}}(\text{CN})_6]$ aqueous solution (40 mM $\text{Na}_4[\text{Fe}^{\text{II}}(\text{CN})_6]$ and 4 M NaCl) at a rate of 60 ml/hour. The latter solution was stirred at 250 rpm with a magnetic stirrer during the instilment. After the instilment, the solutions were stored for 12 hours. Then, the precipitates were filtered through a 0.1- μm filter, washed well with distilled water, and dried in air. The colors of the obtained powders were white (Mn-HCF), blue (Mn/Fe-HCF), light green (Mn/Co-HCF), and light yellow (Mn/Ni-HCF).

The chemical compositions were determined using an inductively coupled plasma (ICP) method and a CHN organic elementary analysis. The weight ratio of the metal elements, *i.e.*, Na, Mn, Fe, Co and Ni, was determined with ICPS-8100 (Shimadzu Ltd.). The samples (ca. 1mg) were dissolved 100 ml of 0.1M HNO_3 aqueous solution. The analytical curves for the respective elements were obtained from the intensity data of the aqueous solutions containing 0, 1, 2, 3, and 5 ppm metal ions. The possible spectral interference was eliminated by high-resolution spectrometer. The percent by weight (wt%) of C, N and H was determined by the CNH analysis. The sample (ca. 100mg) was burned and the produced gases, *i.e.*, CO_2 , NO_2 , and H_2O , were quantitatively analyzed. We determined the wt%s of the constituent elements with assuming that H and O in sample are only H_2O , and listed them in Table I. Under the charge neutrality condition, the chemical formulas of Mn-, Mn/Fe-, Mn.Co-, and Mn/Fe-HCFs become $\text{Na}_{4y-2}\text{Mn}^{\text{II}}[\text{Fe}^{\text{II}}(\text{CN})_6]_{yz}\text{H}_2\text{O}$, $\text{Na}_{4y-2}\text{Mn}^{\text{II}}_{1-x}\text{Fe}^{\text{II}}_x[\text{Fe}^{\text{II}}(\text{CN})_6]_{yz}\text{H}_2\text{O}$, $\text{Na}_{4y-2}\text{Mn}^{\text{II}}_{1-x}\text{Co}^{\text{II}}_x[\text{Fe}^{\text{II}}(\text{CN})_6]_{yz}\text{H}_2\text{O}$, and $\text{Na}_{4y-2}\text{Mn}^{\text{II}}_{1-x}\text{Ni}^{\text{II}}_x[\text{Fe}^{\text{II}}(\text{CN})_6]_{yz}\text{H}_2\text{O}$, respectively. The parameters, x , y , and z , are determined by the least-squares method between the observed and calculated wt%s of the constituent elements. The chemical compositions were $\text{Na}_{1.44}\text{Mn}^{\text{II}}[\text{Fe}^{\text{II}}(\text{CN})_6]_{0.86}2.8\text{H}_2\text{O}$ (Mn-HCF), $\text{Na}_{1.44}\text{Mn}^{\text{II}}_{0.72}\text{Fe}^{\text{II}}_{0.28}[\text{Fe}^{\text{II}}(\text{CN})_6]_{0.86}4.1\text{H}_2\text{O}$ (Mn/Fe-HCF), $\text{Na}_{1.88}\text{Mn}^{\text{II}}_{0.75}\text{Co}^{\text{II}}_{0.25}[\text{Fe}^{\text{II}}(\text{CN})_6]_{0.97}3.4\text{H}_2\text{O}$ (Mn/Co-HCF), and $\text{Na}_{1.64}\text{Mn}^{\text{II}}_{0.74}\text{Ni}^{\text{II}}_{0.26}[\text{Fe}^{\text{II}}(\text{CN})_6]_{0.91}3.9\text{H}_2\text{O}$ (Mn/Ni-HCF).

2.2 Characterization of the as-grown sample

The Synchrotron-radiation X-ray powder diffraction (SR-XRD) measurements were performed at the BL02B2 beamline [13] of SPring-8. The powder samples were filled into 0.3-mm ϕ boro-silicate capillaries and were placed on a Debye-Scherrer camera. The exposure time was 5 min. The X-ray wavelength ($= 0.69923 \text{ \AA}$) was calibrated using the lattice constant of standard CeO_2 powders. The X-ray absorption near-edge structure (XANES) measurements were performed at the BL01B1 beamline of SPring-8. The powder samples were filled into 0.3-mm ϕ boro-silicate capillaries and the X-ray absorption spectra were obtained in a transmission configuration.

The transmission electron microscopy (TEM) images of the samples were obtained with JEM-ARM200F-G (JEOL Ltd.) at an acceleration voltage of 200 kV. In the TEM measurements, the sample powders were dispersed on the micro grid. The TEM images with high spatial resolution are not suitable for evaluation of particle size and its distribution. To evaluate the particle size, scanning

electron microscopy (SEM) images with low spatial resolution were obtained with Mighty-8DX (Vert-me). In the SEM measurements, the powder samples were attached with a silver paste on the sample holder. Then, the sample holder was dried in vacuum for several hours.

2.3 Electrochemical properties

The electrochemical properties were investigated in a beaker-type cell under Ar atmosphere in an Ar filled glove box. The anode was Na metal, and the electrolyte was 1 M NaClO₄ in propylene carbonate (PC). To obtain the cathode electrode, a mixture of a sample, acetylene black, and polyvinylidene difluoride (PVDF) (= 7 : 2 : 1 in weight ratio) was pasted on an Al foil. The electrode thicknesses were 11 - 15 μm. The active area of the film was 1.0 cm². The typical mass of the sample was ~ 0.15mg/cm². We confirmed that the battery performance is nearly independent of the mass of the sample. The upper and lower cut-off voltages were 4.2 and 2.0 V, respectively. During the rate performance measurements, the charge rate was fixed at 0.1 C. During the cycle dependence measurements, the charge and discharge rates were fixed at 0.3 C. We assembled two set of the battery cells for respective samples and confirmed the reproducibility of the electrochemical properties.

3. Results

3.1 Characterization of the as-grown sample

Figure 1 shows SR-XRD patterns of the as-grown samples. All diffraction peaks of Mn-, Mn/Co-, and Mn/Ni-HCFs can be indexed in the trigonal ($R\bar{3}c$; $Z = 3$) structure. The trigonal structure is consistent with the results reported in the literature. [14, 15, 16] In Mn/Fe-HCF, the peaks can be indexed in the face-centered cubic ($Fm\bar{3}m$; $Z = 4$) structure. The lattice constants were refined using the Rietveld method (Rietan-FP [17]): $a_H = 7.5309(6)$ Å and $c_H = 17.915(1)$ Å in Mn-HCF, $a_H = 7.5206(6)$ Å and $c_H = 17.780(1)$ Å in Mn/Co-HCF, $a_H = 7.4916(4)$ Å and $c_H = 17.804(1)$ Å in Mn/Ni-HCF, and $a = 10.4886(5)$ Å in Mn/Fe-HCF.

Figure 2 shows TEM images of the samples. The partial-substitution process reduces the particle size. To evaluate the particle size, SEM images with low spatial resolution were obtained with Mighty-8DX (Vert-me). We evaluated the averages (d) and standard deviations (σ) of the particle size based on the SEM images: $d = 145$ and $\sigma = 30$ nm in Mn-HCF, 92 and 21 nm in Mn/Fe-HCF, 84 and 11 nm in Mn/Co-HCF, and 86 and 13 nm in Mn/Ni-HCF. We further evaluate the grain size from the (002)_C and (012)_H reflections in the SR-XRD patterns (Fig. 1) with use of the Scherrer equation. Considering the angular resolution of the Debye-Scherrer camera (0.03 degree), the grain sizes are estimated to be ≈ 120 nm in Mn-HCF and ≈ 70 nm in Mn/Fe-, Mn/Co-, Mn/Ni-HCFs. These grain sizes are consistent with the particle sizes.

Figure 3 shows XANES around the K-edges of the metal elements: (a) Mn K-edge, (b) Fe K-edge, (c) Co K-edge, and (d) Ni K-edge. The Mn K spectra of the substituted Mn-HCFs are the same as

those of the Mn-HCF [Fig. 3(a)], indicating that Mn takes a high-spin divalent state in the substituted compounds. Similarly, the Fe K spectra of the Mn/Ni- and Mn/Co-HCFs is the same as those of the Mn-HCF [Fig. 3(b)], indicating that $[\text{Fe}(\text{CN})_6]$ takes a low-spin divalent state in the substituted compounds. It is difficult to argue the electronic state of Fe of the Mn/Fe-HCF, because its XANES spectrum due to the substituted Fe is overlapped by that due to $[\text{Fe}(\text{CN})_6]$. The Co K spectrum of the Mn/Co-HCF shows a main peak at the same position as that of $\text{Na}_{1.6}\text{Co}^{\text{II}}[\text{Fe}(\text{CN})_6]_{0.9}$ [Fig. 3(c)], indicating that the substituted Co takes a high-spin divalent state. The Ni K spectrum of the Mn/Ni-HCF is similar to that of $\text{Na}_{0.72}\text{Ni}^{\text{II}}[\text{Fe}(\text{CN})_6]_{0.68}$ [Fig. 3(d)], suggesting that the substituted Ni takes a high-spin divalent state. Thus, the XANES analysis revealed that Mn, Co, and Ni take high-spin divalent states in Mn-, Mn/Co-, Mn/Fe- and Mn/Ni-HCFs.

3.2 Electrochemical properties

Figure 4 shows the rate dependence of the discharge curves. The observed discharge capacity values (Q) at 0.1 C are 116 mAh/g, 119 mAh/g, 134 mAh/g, and 139 mAh/g for Mn-HCF, Mn/Fe-HCF, Mn/Co-HCF, and Mn/Ni-HCF, respectively. These values are close to the ideal values: 120 mAh/g (Mn-HCF), 112 mAh/g (Mn/Fe-HCF), 137 mAh/g (Mn/Co-HCF), and 122 mAh/g (Mn/Ni-HCF). In the non-substituted sample [Fig. 5(a)], Q decreases rapidly as the rate varies from 115 mAh/g at 0.1 C to 16 mAh/g at 10 C, and eventually disappears above 20 C. The partial substitution significantly enhances the rate performance. For example, Q (= 29 mAh/g) is discernible even at 50 C in Mn/Fe-HCF [Fig. 4(b)]. Similar improvements are observed in Mn/Co-HCF [Fig. 4(c)] and Mn/Ni-HCF [Fig. 4(d)]. The broken curves represent discharge curve at 0.1 C after the rate performance measurement. The curves indicate that the rate performance measurements cause slight damages in Mn- and Mn/Ni-HCFs.

Figure 5 shows the cycle dependence of the charge and discharge curves. In the non-substituted sample [Fig. 5(a)], Q decreases rapidly as the rate varies from 103 mAh/g in the first cycle to 52 mAh/g in the fiftieth cycle. That is, Q decreases by 50 % in the fiftieth cycle. The partial substitution significantly enhances the cycle performance. For example, Q decreases only 12 % in the fiftieth cycle in Mn/Fe-HCF [Fig. 5(b)]. Similar improvements are observed in Mn/Ni-HCF [Fig. 5(c)].

Open symbols in Fig. 6(a) show the rate dependence of the relative capacity (Q/Q_0 ; Q_0 is the value at 0.1 C). As indicated by the curves drawn to guide the eye, the partial substitution significantly enhances the rate performance. The enhancement is the most significant in Mn/Ni-HCF. Closed symbols in Fig. 6(a) show the rate performances of another set of the battery cells. The rate performances are nearly the same as the first set of the battery cells. Figure 4(b) shows the cycle dependence of Q/Q_0 (Q_0 is the value in the first cycle). It can clearly be seen that the partial substitution also enhances the cycle performance. The enhancement is significant in Mn/Fe- and Mn/Ni-HCFs.

4. Discussion

Let us consider the possible origins for the enhanced performance by partial substitution of Fe, Co and Ni for Mn in Mn-HCFs. In metal-HCF, the Na⁺ diffusion constant tends to increase with the cell volume.[20] The partial substitution of the smaller metal ions, *i.e.*, Fe²⁺, Co²⁺, and Ni²⁺, for Mn decreases the cell volume of Mn-HCF: 2.9331(4) nm³/chemical formula in Mn-HCF, 2.8825(3) nm³/chemical formula in Mn/Fe-HCF, 2.9029(3) nm³/chemical formula in Mn/Co-HCF, and 2.8844(3) nm³/chemical formula in Mn/Ni-HCF. Therefore, the variation of the Na⁺ diffusion constant cannot explain the enhanced rate performance by partial substitution. Here, we note that the bulk resistivity (ρ) of the metal-HCF is insensitive to the metal element [19]: $\rho = 41 \mu\Omega\text{cm}$ in Na_{1.32}Mn[Fe(CN)₆]_{0.83} and $39 \mu\Omega\text{cm}$ in Na_{1.6}Co[Fe(CN)₆]_{0.9}. This suggests that the electric conductivity of the discharge state is insensitive to the partial substitution of Fe, Co and Ni for Mn in Mn-HCFs. However, we do not know how the partial substitution affects the bulk resistivity in the charge state. In this sense, there still remains the possibility that the resistivity change explains the enhanced performance. Another possible origin for the enhanced performance is the reduced particle size. The partial substitution of Fe, Co and Ni for Mn in Mn-HCFs reduces the particle size from 145 nm to 84 - 92 nm. The smaller size is advantageous for the rate performance and partly explains the enhanced rate performance. The partial substitution further increases the water content of the compounds: Na_{1.44}Mn^{II}[Fe^{II}(CN)₆]_{0.86}·2.8H₂O (Mn-HCF), Na_{1.44}Mn^{II}_{0.72}Fe^{II}_{0.28}[Fe^{II}(CN)₆]_{0.86}·4.1H₂O (Mn/Fe-HCF), Na_{1.88}Mn^{II}_{0.75}Co^{II}_{0.25}[Fe^{II}(CN)₆]_{0.97}·3.4H₂O (Mn/Co-HCF), and Na_{1.64}Mn^{II}_{0.74}Ni^{II}_{0.26}[Fe^{II}(CN)₆]_{0.91}·3.9H₂O (Mn/Ni-HCF). Even though the role of the water in the electrochemical properties is unclear, there remains the possibility that the high water content improves the battery performance.

Figure 7 shows *ex situ* X-ray diffraction (XRD) patterns of the Mn-, Mn/Co, Mn/Ni-, and Mn/Fe-HCFs in the fully discharge and charge states. The battery cell was disassembled under Ar atmosphere in an Ar filled glove box. The cathode electrode on Al foil was sealed in a plastic bag. The incident X-ray was Cu K α line. All diffraction peaks can be indexed in the face-centered cubic (Fm $\bar{3}$ m; $Z = 4$) structure. We note that the Mn-, Mn/Co, and Mn/Ni-HCFs remain cubic even in the fully discharge state after the charge process. The absence of the cubic-trigonal structural phase transition is responsible for the good cycle performance [Fig. 6(b)]. We summarize the lattice constants (a) in the discharge and charge state in Table II. The a value of the Mn-HCF decreases by 0.06 Å reflecting the smaller ionic radius (= 0.65 Å) of Mn³⁺ than that (= 0.83 Å) of Mn²⁺. In contrast, the a values of the Mn/Fe-HCF and Mn/Ni-HCF rather increase. Thus, the substitution of Fe and Ni for Mn significantly influences the lattice response to the Na⁺ intercalation/deintercalation. The difference (Δa) in a is the smallest in Mn/Ni-HCF. This may be responsible for the good cycle performance [Fig. 6(b)]. By the way, the a value of the Mn/Co-HCF decreases by 0.14 Å. This exceptional behavior may be ascribed to the small deficiency (= 3%) of [Fe(CN)₆] and resultant participation of the Co reduction reaction

(Co³⁺/Co²⁺): Na_{1.88}Mn^{II}_{0.75}Co^{II}_{0.25}[Fe^{II}(CN)₆]_{0.97} → Mn^{III}_{0.75}Co^{II}_{0.09}Co^{III}_{0.16}[Fe^{III}(CN)₆]_{0.97} + 1.88Na⁺. We note that the ionic radius (= 0.55 Å) of Co³⁺ is much smaller than that (= 0.75 Å) of Co²⁺.

Figure 8 shows the voltage-derivative (dQ/dV) of the capacity at 0.1 C. In Mn-HCF [Fig. 8(a)], two sharp peaks are observed at ≈ 3.4 V and ≈ 3.7 V in the charge curve (positive side). The former and latter correspond to the Fe and Mn oxidization reactions, respectively. [11] In the discharge curve (negative side), a single broad peak is observed at ≈ 3.3 V. The 3.3 V peak is ascribed to the Fe reduction reaction. This indicates that the Mn reduction reaction is not well activated in Mn-HCF. We emphasize that a clear two-peak feature is observed at ≈ 3.4 V and 3.5 - 3.6 V in the discharge curve of the Mn/Fe-, Mn/Co-, and Mn/Ni-HCFs [Figs. 6(b)-(c)]. This means that the substituted elements activate the Mn reduction reaction. This activation is responsible for the enhanced rate and cycle performances by partial substitution. In the charge curve, the partial substitution makes the peak structure rather broader. Especially, the sharp peak due to the Fe oxidization reaction seems to merge into the broad background structure. Figure 9 shows the rate and cycle dependence of dQ/dV of Mn/Fe-HCF. We found that the peak structure due to Mn reduction reaction becomes weaker with rate and cycle.

A plausible mechanism of the activation of the Mn reduction reaction is as follows. The charge state of Mn-HCF has a high density of Mn³⁺ and is amenable to the cooperative JT distortion. For example, in RbMn^{III}[Fe^{II}(CN)₆][20], a tetragonal ($2^{1/2}a < c$) structure results from a ferro-type JT distortion along the *c* axis. In Li_xMn[Fe(CN)₆]_{0.93}·2.3H₂O ($x < 0.3$),[21] the tetragonal ($2^{1/2}a > c$) structure is ascribed to the antiferro-type JT distortion within the *ab* plane. Even though the Mn-HCF does not show crystallographic tetragonal distortion in the charge state, a cooperative JT distortion is considered to exist locally. The cooperative JT distortion of Mn³⁺ makes the reduction reaction of Mn³⁺ difficult. Alternatively, the reduction process is mediated by an internal charge-transfer from Fe²⁺ to Mn³⁺. [12] Such an indirect process is considered to be very slow. Conversely, the partial substitution of the JT-inactive ions, *i.e.*, Fe²⁺, Co²⁺, and Ni²⁺, suppresses the cooperative JT distortion and activates the Mn reduction reaction. The XANES analysis revealed that Mn, Co and Ni take high-spin divalent states in Mn-, Mn/Co-, Mn/Fe- and Mn/Ni-HCFs. In addition, Fe in Na_{0.92}Fe^{II}[Fe^{II}(CN)₆] is reported to take a high-spin state[7], suggesting that the substituted Fe takes a high-spin divalent state in Mn/Fe-HCF. The ionic radius of high-spin Mn²⁺, high-spin Fe²⁺, high-spin Co²⁺, and high-spin Ni²⁺ are 0.83, 0.78, 0.75, and 0.69 Å, respectively. The smallest substituent (Ni²⁺) most significantly improves the rate performance [Fig. 6(a)].

5. Conclusion

In conclusion, we observed that partial substitution of Fe, Co, and Ni for Mn in Mn-HCF significantly enhances the SIB rate and cycle performance. The substituted elements activates the Mn reduction reaction (Mn³⁺/Mn²⁺) probably by the suppression of the cooperative Jahn-Teller distortion

of Mn³⁺. Thus, partially substituted Mn-HCFs are promising cathode materials for high-power batteries.

Conflict of interest

There are no known conflicts of interest associated with this work.

Acknowledgments

This work was supported by the Yazaki memorial foundation for science and technology and Nippon sheet glass foundation for materials science and engineering. T. S. was supported by the Nanotech Research Professional (NRP) course of Nanotech Career-up Alliance in Nanotech (CUPAL) project. The SRXRD measurements were performed using the BL02B2 beamlines (proposal No. 2015B1077) of SPring-8 with the approval of the Japan Synchrotron Radiation Research Institute (JASRI). The XANES measurements were performed using the BL01B1 beamlines (proposal No. 2015B1076) of SPring-8 with the approval of the Japan Synchrotron Radiation Research Institute (JASRI). The elementary analyses were performed at the Chemical Analysis Division, Research Facility Center for Science and Engineering, University of Tsukuba. The TEM investigation was supported by NIMS microstructural characterization platform (NMCP) as a program of "Nanotechnology Platform" of the Ministry of Education, Culture, Sports, Science and Technology (MEXT), Japan.

References

- [1] A. Ludi, H. U. Güdel, Structural chemistry of polynuclear transition metal cyanides, in *Inorganic chemistry*, Vol. 14, Structure and Bonding, Springer, Berlin, 1973, p. 1.
- A. Ludi, H. U. Guedel, M. Rugg, Structural chemistry of Prussian blue analogues. Single crystal study of manganese (II) hexacyanocobaltate (III), M₃[C₆(CN)₆]₂xH₂O, *Inorg. Chem.* 9 (1970) 2224.
- [2] Y. Lu, L. Wang, J. Cheng, J. B. Goodenough, Prussian blue: a new framework of electrode materials for sodium batteries, *Chem. Commun.* 48 (2012) 6544.
- [3] T. Matsuda, M. Takachi, Y. Moritomo, A sodium manganese ferrocyanide thin film for Na-ion batteries, *Chem. Commun.* 49 (2013) 2750.
- [4] M. Takachi, T. Matsuda, Y. Moritomo, Cobalt hexacyanoferrate as cathode material for Na⁺ secondary battery, *Appl. Phys. Express* 6 (2013) 025802.
- [5] D. Yang, J. Xu, X.-Z. Liao, Y.-S. He, H. Liu, Z.-F. Ma, Structure optimization of prussian blue analogue cathode materials for advanced sodium ion batteries, *Chem. Commun.* 50 (2014) 13377.
- [6] H. W. Lee, R. Y. Wang, M. Oasta, S. W. Lee, N. Liu, Y. Chi, Manganese hexacyanomanganate open framework as a high-capacity positive electrode material for sodium-ion batteries, *Nature Commun.* 5 (2014) 5280.
- [7] L. Wang, J. Song, R. Qiao, La. Wray, La. M. A. Hossain, Y.-D. Chung, W. Yang, Y. Lu, D. Evans,

- J.-J. Lee, S. Vail, X. Zhao, M. Nishijima, S. Kakimoto, J. B. Goodenough, Rhombohedral prussian white as cathode for rechargeable sodium-ion batteries, *J. Am. Chem. Soc.* 137 (2015) 2548.
- [8] S. Yu, Y. Li, Y. Lu, B. Xu, Q. Wang, M. Yan, Y. Jing, A promising cathode material of sodium iron-nickel hexacyanoferrate for sodium ion batteries, *J. Power Sources* 275 (2015) 45.
- [9] Y. You, X.-L. Wu, Y.-X. Yin, Y.-G. Guo, High-quality prussian blue crystals as superior cathode materials for room-temperature sodium-ion batteries, *Energy Environ. Sci.* 7 (2014) 1643.
- [10] P. Xiao, J. Song, L. Wang, J. Goodenough, and G. Henkelman, Theoretical study of the structural evolution of a $\text{Na}_x\text{FeMn}(\text{CN})_6$ cathode upon Na intercalation, *Chem. Mater.* 27 (2015) 3763.
- [11] M. Takachi, T. Matsuda, Y. Moritomo, Redox reactions in prussian blue analogues against Li concentration, *Jpn. J. Appl. Phys.* 52 (2013) 090202.
- [12] Y. Moritomo, K. Wakaume, M. Takachi, X. H. Zuo, H. Kamioka, Li^+ intercalation of manganese hexacyanoferrate as investigated by in situ valence-differential absorption spectroscopy, *J. Appl. Phys.* 52 (2013) 017301.
- [13] E. Nishibori, M. Takata, K. Kato, M. Sakata, Y. Kubota, S. Aoyagi, Y. Kuroiwa, M. Yamakawa, N. Ikeda, The large Debye-Scherrer camera installed at SPring-8 bl02b2 for charge density studies, *J. Phys. Chem. Solids* 62 (2001) 2095.
- [14] Y. Moritomo, Y. Kurihara, T. Matsuda, J. E. Kim, Structural phase diagram of Mn-Fe cyanide against cation concentration, *J. Phys. Soc. Jpn.* 80 (2011) 103601.
- [15] Y. Moritomo, T. Matsuda, Y. Kurihara, J. E. Kim, Cubic-rhombohedral phase transition in $\text{Na}_{1.32}\text{Mn}[\text{Fe}(\text{CN})_6]_{0.833}\cdot 3.6\text{H}_2\text{O}$, *J. Phys. Soc. Jpn.* 80 (2011) 074608.
- [16] Y. Moritomo, T. Matsuda, Y. Kurihara, J. E. Kim, Erratum: "cubic-rhombohedral structural phase transition in $\text{Na}_{1.32}\text{Mn}[\text{Fe}(\text{CN})_6]_{0.833}\cdot 3.6\text{H}_2\text{O}$ ", *J. Phys. Soc. Jpn.* 85 (2016) 039001.
- [17] F. Izumi, K. Momma, Three-dimensional visualization in powder diffraction, *Solid State Phenom.* 130 (2007) 15.
- [18] Y. Moritomo, M. Takachi, Y. Kurihara, T. Matsuda, Thin film electrode of prussian blue analogues with rapid Li^+ intercalation, *Appl. Phys. Express* 5 (2012) 041801.
- [19] Y. Kurihara, Y. Moritomo, Fabrication of epitaxial interface between transition metal cyanides, *Jpn. J. Appl. Phys.* 50 (2011) 060210.
- [20] M. Takachi, Y. Fukuzumi, Y. Moritomo, Na^+ diffusion kinetics in nanoporous metal-hexacyanoferrates, *Dalton Trans.* 45 (2016) 458.
- [20] K. Kato, Y. Moritomo, M. Takata, M. Sakata, M. Umekawa, N. Hamada, S. Ohkoshi, H. Tokoro, K. Hashimoto, Direct observation of charge transfer in double-perovskite-like $\text{RbMn}[\text{Fe}(\text{CN})_6]$, *Phys. Rev. Lett.* 91 (2003) 255502.
- [21] Y. Kurihara, T. Matsuda, Y. Moritomo, Structural properties of manganese hexacyanoferrate against Li concentration, *Jpn. J. Appl. Phys.* 52 (2013) 017301.

Figure captions

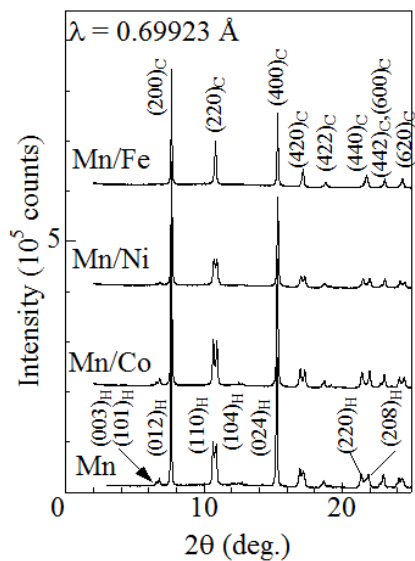


Fig. 1: X-ray diffraction patterns of as-grown Mn-, Mn/Co-, Mn/Ni-, and Mn/Fe-HCFs. The wavelength of the incident X-ray was 0.69923 Å. Values in parentheses represent indexes in the face-centered cubic (C) or trigonal (H; hexagonal setting) structures.

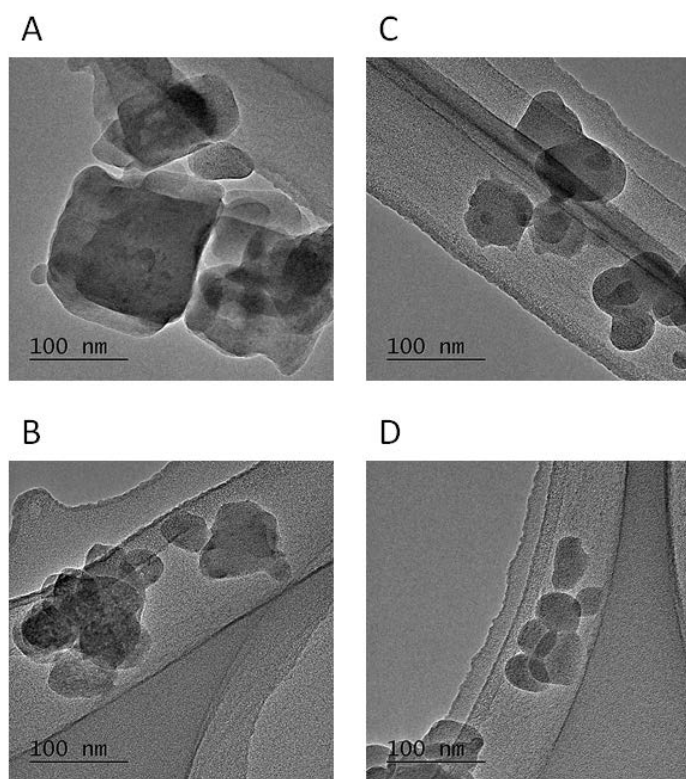


Fig. 2: Transmission electron microscopy (TEM) images of as-grown (a) Mn-, (b) Mn/Fe-, (c) Mn/Co-, and (d) Mn/Ni-HCFs.

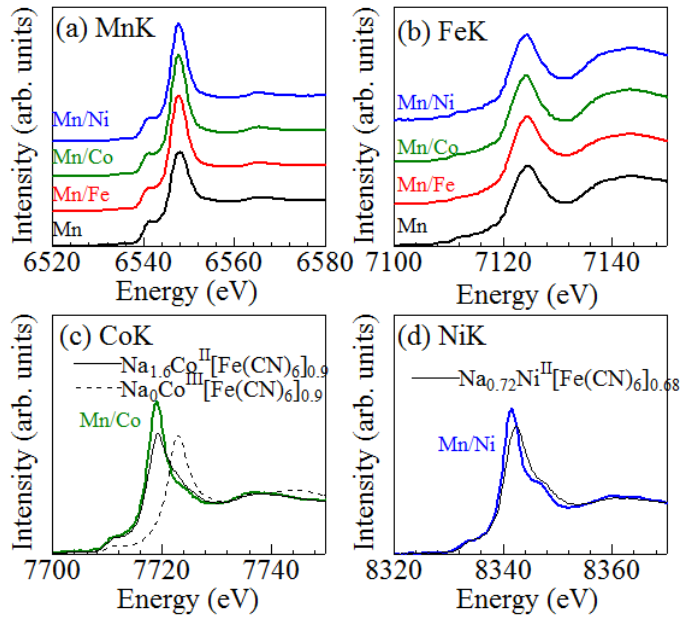


Fig. 3: X-ray absorption near-edge structure (XANES) around the transition metal K-edge of as-grown Mn-, Mn/Fe-, Mn/Co-, and Mn/Ni-HCFs.: (a) Mn K-edge, (b) Fe K-edge, (c) Co K-edge, and (d) Ni K-edge. The spectra of $\text{Na}_{1.6}\text{Co}^{\text{II}}[\text{Fe}(\text{CN})_6]_{0.9}$ and $\text{Na}_0\text{Co}^{\text{III}}[\text{Fe}(\text{CN})_6]_{0.9}$ are replotted from Ref. 11. The spectrum of $\text{Na}_{0.72}\text{Ni}^{\text{II}}[\text{Fe}(\text{CN})_6]_{0.68}$ is replotted from Ref. 18.

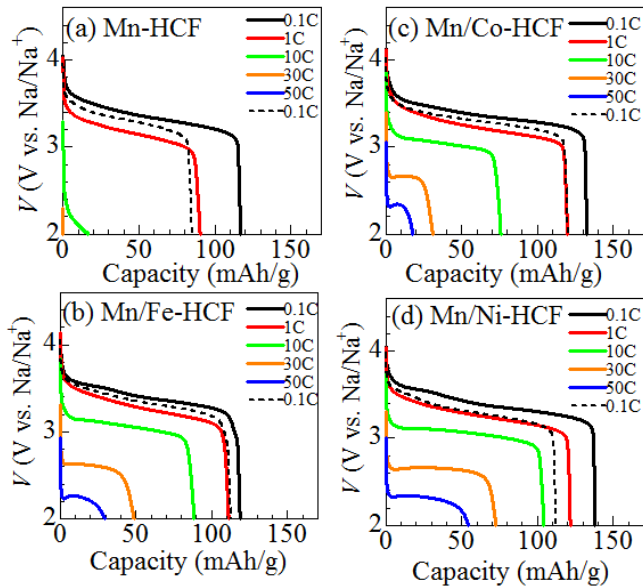


Fig. 4: Rate dependence of discharge curves in (a) Mn-, (b) Mn/Fe-, (c) Mn/Co-, and (d) Mn/Ni-HCFs. The charge rate was fixed at 0.1 C. The broken curves represent discharge curve at 0.1 C after the rate performance measurement.

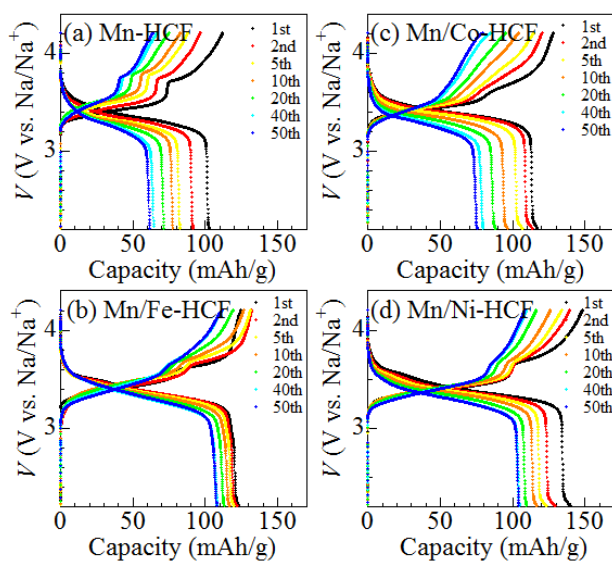


Fig. 5: Cycle dependence of charge and discharge curves in (a) Mn-, (b) Mn/Fe-, (c) Mn/Co-, and (d) Mn/Ni-HCFs. The charge rate was fixed at 0.3 C.

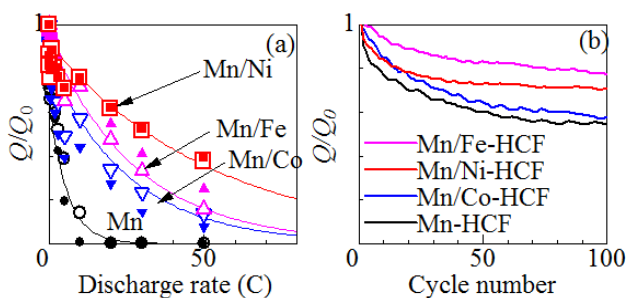


Fig. 6: (a) Relative discharge capacity (Q/Q_0 ; Q_0 is the value at 0.1 C) against the discharge rate. Open and closed symbols represent the rate performances of the first and second sets of the battery cells, respectively. Solid curves are drawn for the open symbols merely to guide the eye. (b) Q/Q_0 (Q_0 is the value in the first cycle) against the cycle number. The charge and discharge rates were fixed at 0.3 C.

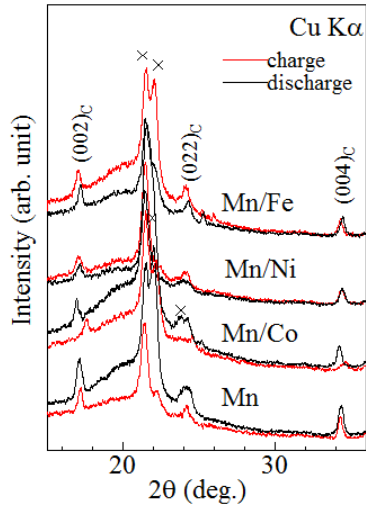


Fig. 7: X-ray diffraction patterns of Mn-, Mn/Co-, Mn/Ni-, and Mn/Fe-HCFs in the fully discharge and charge states. The incident X-ray was Cu $K\alpha$ line. Values in parentheses represent indexes in the face-centered cubic (C) structures. Crosses represent the diffraction peaks due to Al foil or sample holder.

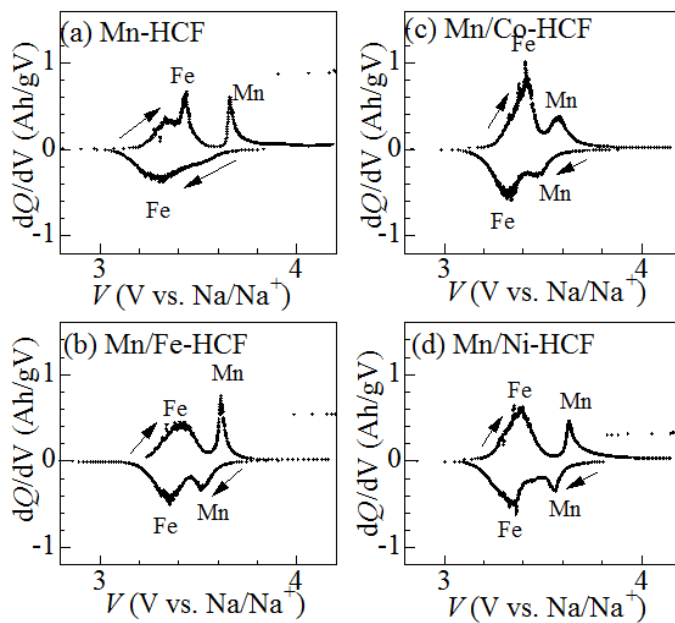


Fig. 8: Voltage derivative of capacity (dQ/dV) at 0.1 C in (a) Mn-, (b) Mn/Fe-, (c) Mn/Co-, and (d) Mn/Ni-HCFs. Fe and Mn represent the redox reactions of the elements.

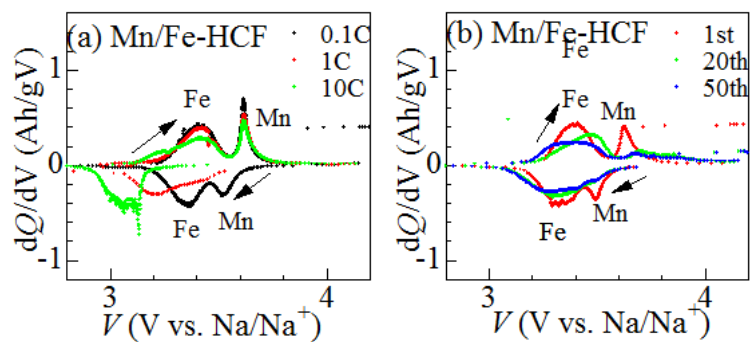


Fig. 9: (a) Rate and (b) cycle dependence of dQ/dV of Mn/Fe-HCF. Fe and Mn represent the redox reactions of the elements.

Table caption

compound	Na	Mn	Fe	Co	Ni	C	H	N
Mn/Fe-HCF	9.86 ± 0.06	16.84 ± 0.10	19.02 ± 0.06	---	---	19.06	1.85	22.24
Mn/Ni-HCF	10.47 ± 0.06	11.45 ± 0.07	14.21 ± 0.04	---	4.09 ± 0.04	18.34	2.20	21.40
Mn/Co-HCF	11.45 ± 0.06	14.02 ± 0.08	15.32 ± 0.05	3.78 ± 0.04	---	18.02	2.39	21.02
Mn-HCF	11.40 ± 0.06	17.03 ± 0.10	14.95 ± 0.08	---	---	19.30	1.76	22.51

Table I: Percent by weight of the constituent elements in Mn-, Mn/Co, Mn/Ni- and Mn/Fe-HCFs.

compound	a in discharge state	a in charge state	Δa
Mn/Fe-HCF	10.35 Å	10.42 Å	+0.07 Å
Mn/Ni-HCF	10.40 Å	10.41 Å	+0.01 Å
Mn/Co-HCF	10.45 Å	10.31 Å	-0.14 Å
Mn-HCF	10.40 Å	10.34 Å	-0.06 Å

Table II: Lattice constant (a) of Mn-, Mn/Co, Mn/Ni- and Mn/Fe-HCFs in the discharge and charge states. Difference (Δa) in a between the two states are also listed.